

<https://doi.org/10.1038/s44310-025-00068-3>

Fast 3D localization of nano-objects in wide-field interferometric scattering microscopy via vectorial diffraction model-derived analytical fitting

Check for updates

Liaoliao Wei¹, Caroline Livan Anyi¹, Huakun Li¹, Haitao Nie², Bihan Wen³ & Tong Ling^{1,3,4,5} ✉

Interferometric scattering microscopy (iSCAT) enables tracking single nano-objects in three dimensions (3D). Conventional image processing methods for 3D localization in iSCAT typically rely on template matching, which involves finding the maximum cross-correlation with modeled interferometric point spread functions (iPSFs). However, this approach can be computationally intensive and hinders the processing of nano-object movements on a large scale. In this study, we introduce an efficient analytical fitting approach for retrieving the 3D positions of nano-objects in wide-field iSCAT. We derive an approximate analytic iPSF model based on the Richards-Wolf vectorial diffraction model. The simplified analytic function includes a quadratically scaling amplitude term and a linearly scaling phase term, both of which change with the nano-object's axial position. After using the Bayesian estimation method to obtain initial parameters, we can retrieve the axial location of the nano-object through univariate least squares fitting, achieving a 60- to 200-fold increase in processing speed compared with template matching. Intriguingly, we also show that without approximation, least squares fitting can yield higher precision than cross-correlation. We validate the proposed method by measuring the movements of static and moving nanoparticles in multiple experiments. In particular, we record the movements of nanoparticles on the order of tens of nanometers accompanying the thermal expansion of a polydimethylsiloxane (PDMS) substrate. The retrieved nanoparticle displacement matches the estimated expansion from finite element modeling. By combining precise Bayesian estimation of the fixed parameters and analytical fitting in which the only variable is the nano-object's axial position, our method enables high-throughput 3D tracking of nano-objects in a wide field of view. This approach may benefit label-free monitoring of nano-objects (such as nanoparticles, exosomes, and viruses) on a large scale.

Interferometric scattering microscopy (iSCAT) has become a powerful imaging technique that enables detecting and tracking individual nano-objects, including nanoparticles, viruses, and proteins^{1–5}. iSCAT utilizes common-path interferometry to enhance the signal contrast of scattered light, facilitating highly sensitive quantitative analysis of nano-objects. The interference between the reference and scattered light produces the

interferometric point spread function (iPSF) pattern in the form of intensity signal captured by the camera. The iPSF contains information about the nano-object's scattering amplitude and phase, which encodes the defocus of the object and the relative optical path difference (OPD) with respect to the reference plane (typically the upper surface of the glass coverslip)⁶.

¹School of Chemistry, Chemical Engineering and Biotechnology, Nanyang Technological University, Singapore, Singapore. ²Department of Electrical and Electronic Engineering, The University of Hong Kong, Pokfulam, Hong Kong SAR, China. ³School of Electrical and Electronic Engineering, Nanyang Technological University, Singapore, Singapore. ⁴SERI-NTU Advanced Ocular Engineering (STANCE) Program, Singapore, Singapore. ⁵Singapore Eye Research Institute, Singapore National Eye Centre, Singapore, Singapore. ✉e-mail: tong.ling@ntu.edu.sg

As such, several studies have pioneered axial localization of nano-objects using iSCAT^{7–10}. The most common approach involves generating iPSF templates corresponding to all possible parameter sets using a physical model, such as the Richards-Wolf integral model^{11–16}, and finding the best-matched iPSF pattern within this library by cross-correlation against the experimentally captured iPSF^{6,17–21}. For simplicity, we will refer to this method as *template matching*. Besides the fundamental limit set by the shot noise, the localization sensitivity of the template matching approach is also limited by the discrete sampling interval of the iPSF templates in the axial direction. Therefore, 3D localization using template matching often requires constructing a large library of iPSF patterns with sufficient granularity while covering a wide parameter range. The process of finding the best match thus necessitates iterating through all possible parameter sets of the modeled iPSFs, which can be computationally intensive and time-consuming.

Besides template matching, localization of single nano-objects in iSCAT can be treated as an estimation problem in the realm of statistics, particularly for maximizing localization accuracy. While maximum likelihood estimation was often used to localize fluorescent molecules in single-molecule localization microscopy^{22–24}, de Wit et al. showcased a Bayesian parameter estimation framework for the 3D localization of single nano-objects in iSCAT that incorporated prior information about parameter distributions⁷. This method can also quantify correlations between parameters, such as the scattering phase and the nanoparticle’s axial position, and their marginalized uncertainty. However, this statistical approach requires a relatively resource-intensive sampling of the posterior using the Markov chain Monte Carlo (MCMC) method^{25,26}. Similar to template matching, the Bayesian estimation method would fall short if a fast-processing time is essential for high-throughput extraction of nanoparticle locations across a large field of view (FOV).

In this paper, we present a method that combines Bayesian estimation and analytical fitting to enhance the efficiency of 3D localization of nano-objects in iSCAT, while the 3D localization task is divided into two more manageable sub-problems: lateral localization in (x, y) and axial localization in z . Regarding lateral localization, we employ the radial variance transform (RVT) method to convert the iPSF pattern from concentric rings into a single bright spot²⁷. Subsequently, the *trackpy* algorithm is used to dynamically track the lateral position of the nano-object²⁸. For the axial localization, we derive an approximate iPSF model based on the Richards-Wolf integral, which turns the iPSF pattern into a univariate analytic function of the nano-object’s axial location z_p . Such a function allows axial localization

via direct analytical fitting, while other necessary parameters can be determined in advance using the Bayesian estimation method. We utilize least squares as the loss function to fit the model to the experimental iPSF pattern. The analytical fitting approach was validated through multiple simulations and experiments, demonstrating its applicability and precision in both static and dynamic tracking scenarios.

Results

Vectorial diffraction model-derived iPSF analytic function for fast axial localization

The schematic diagram of iSCAT under wide-field illumination is illustrated in Fig. 1a, with a camera capturing the interference pattern between the reference light reflected by the top surface of the coverslip and the scattered light from the nano-object. The intensity detected on the camera can be formulated as follows:

$$I = |E_{\text{ref}}|^2 + |E_{\text{sca}}|^2 + 2|E_{\text{ref}}||E_{\text{sca}}|\cos\Delta\varphi \quad (1)$$

where I is the intensity detected by the camera, E_{ref} is the reference field reflected by the coverslip’s top surface, E_{sca} is the scattered field from the nano-object, and $\Delta\varphi$ is the phase difference between the reference and the scattered field.

Previous studies have shown that iPSF patterns can be accurately modeled using the Richards-Wolf integral^{6,8,11}. This precise vectorial diffraction model allows for separate generation of amplitude and phase maps, as illustrated in Fig. 1a, which demonstrates that both amplitude and phase vary with changes in the nanoparticle’s axial position z_p . Consequently, the location information can be extracted from both amplitude and phase, a process achievable through the proposed analytical model described in the following Eq. (2).

In a low NA iSCAT imaging system, the small beam angle ensures that polarization effects are minimal. Therefore, the vectorial scattered field E_{sca} can be approximated to an analytic function of the nanoparticle’s axial position z_p parameterized by the focus position z_f , numerical aperture NA, wave number k , etc. that are fixed during the recording (see Supplementary Methods, Section I - III), where

$$E_{\text{sca}}(r, z_p) = -iE_{s0} \cdot J'(r) \cdot A(z_p) \cdot e^{i\Phi(z_p)} \quad (2)$$

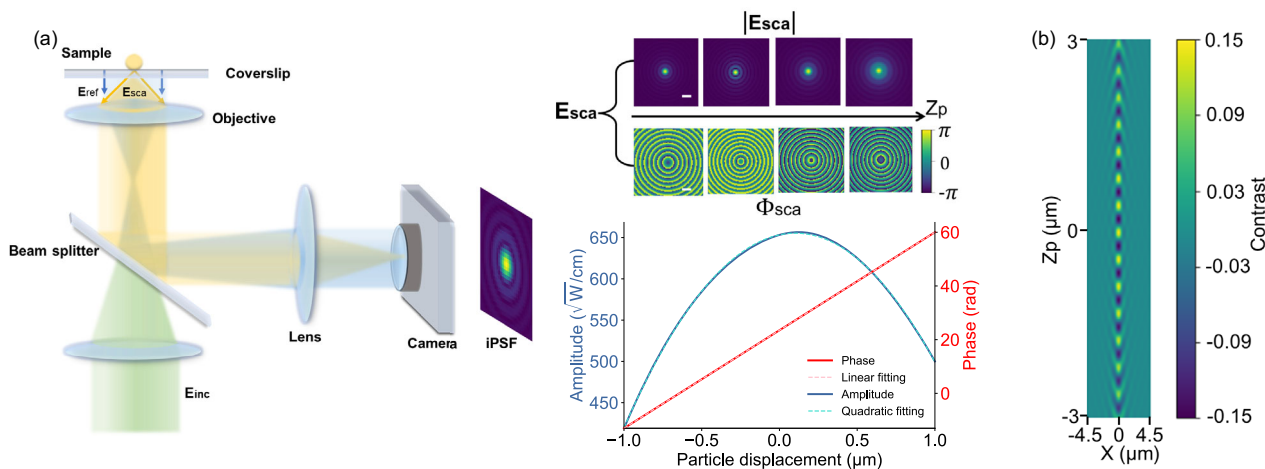


Fig. 1 | Diagrams of a wide-field iSCAT and simulated iPSFs. **a** Schematic diagram of a wide-field iSCAT imaging system. The amplitude and phase variations of the scattered field, as predicted by the Richards-Wolf model, are presented as functions of particle displacement in both two-dimensional (2D) (upper) and one-dimensional (1D) (lower) representations. The 1D plot is derived from the center point of the scattered field as an example. Notably, all points within the scattered field

follow a quadratic amplitude change and a linear phase change with respect to the particle displacement, consistent with the theoretical predictions of the Richards-Wolf integral model. Scale bar: 2 μm. **b** A low NA example (NA = 0.5) of the meridional profile of the iPSFs as a function of the nanoparticle’s axial position z_p , showing periodic intensity variations with the peak intensity gradually decreasing as $|z_p|$ increases.

where $E_{\text{sca}}(r, z_p)$ is the simplified scalar scattered field. $J'(r)$ is a superposition of modified zero-order Bessel function across all beam angles (see Supplementary Methods, Section III), while r refers to the distance from an arbitrary point on the image plane to the center point. E_{s0} is a scaling factor proportional to the complex polarizability of the particle and the wave number of the incident field⁶.

In the approximate model, the amplitude term A exhibits a quadratic relationship with respect to the particle axial position z_p and system defocus z_f , which can be derived as

$$A(z_p) = \begin{bmatrix} z'^2 & z' & 1 \end{bmatrix} \cdot \begin{bmatrix} -\frac{k^2}{2} \\ ik \\ 1 \end{bmatrix}, \quad (3)$$

where

$$z' = n'_p z_p + n'_f z_f. \quad (4)$$

Meanwhile, $\Phi(z_p)$ exhibits a linear correlation with z_p , in which

$$\Phi(z_p) = k \cdot (n_p z_p + n_f z_f). \quad (5)$$

For simplicity, n'_p and n'_f are defined as the effective refractive indices in the amplitude term, n_p and n_f are defined as the effective refractive indices in the phase term. The detailed expressions of the effective refractive indices and the derivation can be found in Supplementary Methods, Section I-III, Eqs. (S8-S32).

To validate the feasibility of the proposed analytical model in Eq. (2), which represents the interferometric point spread function (iPSF) as a combination of a linear phase term and a quadratically scaling amplitude term, simulations were performed using the original Richards-Wolf integral model. Figure 1a visualizes the unwrapped phase shift²⁹ and the amplitude variation with respect to the nanoparticle's axial position z_p . The unwrapped iPSF pattern's phase and amplitude variations closely match linear and quadratic functions, respectively, as indicated by the dashed lines, demonstrating consistency with the proposed model. Figure 1b presents a

meridional profile of the iPSFs as a function of z_p , further supporting the model's validity by revealing periodic intensity changes attributed to the linear phase change with z_p and a gradual decrease in peak intensity as $|z_p|$ increases, primarily due to the quadratic relationship between the amplitude and z_p .

For axial localization of nano-objects, we assumed a constant system defocus z_f during the nano-objects' movement. Consequently, we were able to estimate z_f and other system parameters using the Bayesian estimation method in advance. Once the z_f is known, the modeled iPSF pattern \hat{I} became a function of a single variable, z_p . We employed least squares estimation (LSE)³⁰ to retrieve z_p by fitting the modeled iPSF pattern $\hat{I}(r, z_p)$ to the experimental one $I(r)$. The error ϵ should satisfy the following requirement:

$$\epsilon(z_p) = \min_{z_p} \|\hat{I}(r, z_p) - I(r)\|_F^2 \quad (6)$$

where $\|\cdot\|_F$ represents the Frobenius norm³¹.

Nanometer-scale precision and large dynamic range achieved by the analytical fitting method in localizing nanoparticles under wide-field iSCAT

We validated the feasibility of the proposed analytical fitting method and compared its performance with conventional template matching method through simulations (Supplementary Methods, Section IV), demonstrating a superior efficiency and sensitivity. The proposed method outperformed conventional approaches in speed by ~100 folds (Table S1) and exhibited higher sensitivity than cross-correlation under low signal-to-noise ratio (SNR) conditions (<10 dB) (Fig. S3). Meanwhile, the localization error between the proposed approximate model and the ground truth was <2 nm for NAs lower than 0.8, indicating high degrees of similarity between the two models (Fig. S2).

To validate the sensitivity of the proposed method under experimental conditions, static iPSF patterns of 200 nm nanoparticles were recorded at a frame rate of 1 kHz over a duration of 10 s. Figure 2a presents an image extracted from the video, where the iPSF patterns are sparsely distributed across the FOV. The inset of Fig. 2a provides an example of the fitting result. Since the particles were static, their axial positions were expected to remain

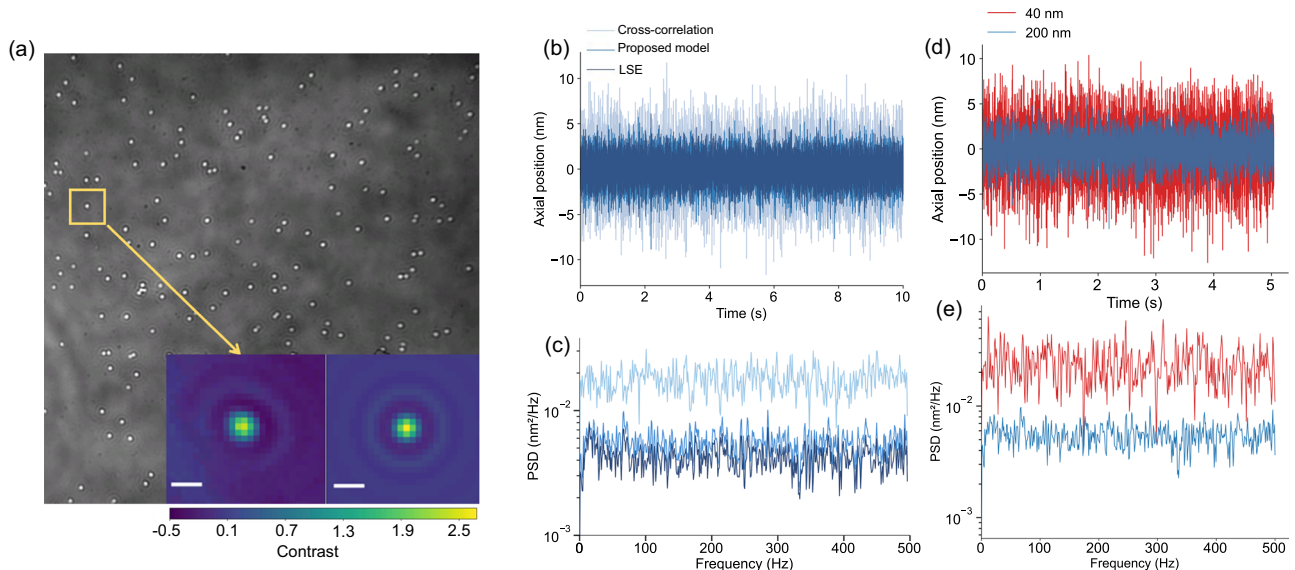
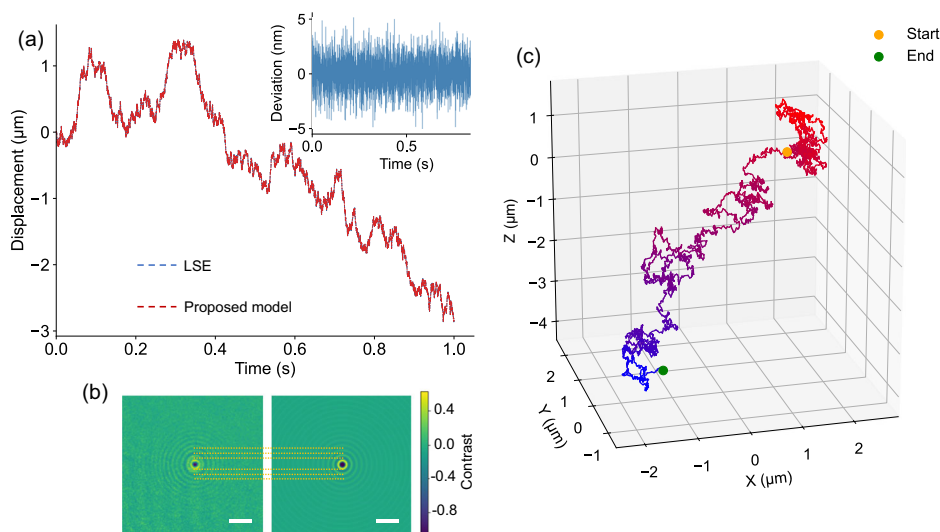


Fig. 2 | Fitting results in the static situation. **a** An extracted frame from the recorded experiment video with a $48 \mu\text{m} \times 48 \mu\text{m}$ FOV. Inset: a single iPSF pattern from the experimental data (left) and its corresponding 2D fitting data obtained using the proposed analytical model (right). Scale bar in inset: $1 \mu\text{m}$. **b** Comparison of axial position fluctuations estimated using template-matching methods and the

proposed analytical model fitting approach. **c** PSD of the axial position fluctuations presented in **(b)**. **d** Comparison of axial position fluctuations in imaging 200 nm nanoparticles and 40 nm nanoparticles. **e** PSD of the axial position fluctuations presented in **(d)**.

Fig. 3 | Dynamic tracking of the particle movement. **a** The axial displacement trajectory in 1 s estimated by the proposed analytical fitting approach and template matching using LSE. Inset: the difference between the axial localization results using the two methods. **b** A 2D fitting example comparing the experiment iPSF (left) and the fitted iPSF (right). Scale bar: 2 μm . **c** The 3D trajectory of the particle diffusion in water.



constant. We assessed possible focus drift over the 10-s recording using Bayesian estimation and observed minimal variation (~ 3 nm), which validated the assumption of a constant system defocus during the recording. The performance of the proposed method was compared to conventional template matching using cross-correlation. Furthermore, template matching with LSE, selected as the loss function in this study, was also included as a benchmark for comparison. The robustness of localization was assessed across three methods: cross-correlation template matching, LSE template matching, and analytical model fitting. Over 10,000 frames, the standard deviation of localization fluctuation was 1.6 nm for the proposed approach, 3.0 nm for the cross-correlation template-matching, and 1.4 nm for the LSE template-matching. These results demonstrate the high reliability of the proposed method and confirm the feasibility of using LSE as the loss function. The fluctuation and power spectrum density (PSD) curves are presented in Figs. 2b, c.

For a region of interest (ROI) of 27×27 pixels in size, the proposed analytical model achieved a fitting speed of ~ 200 frames per second on an Intel Xeon Gold 6330 CPU and ~ 700 frames per second on an Apple M2 CPU (Table S2). In contrast, conventional template matching was running at a speed of approximately 3.3 frames per second on an Intel Xeon Gold 6330, making it 60 times slower than the fitting-based approach, which highlights the significant advantage of the proposed fitting model for high-throughput particle localization. The size of the ROI is a critical factor influencing image processing speed, as an increase in the pixel count directly leads to longer processing times. On the other hand, too small ROI sizes may result in truncating the iPSF pattern, wasting a substantial portion of the signal energy and reducing the localization precision.

Considering the practical application and generalizability of the proposed method, we also evaluated its performance in localizing small nanoparticles. We selected gold nanoparticles with a diameter of 40 nm for our study as it was previously demonstrated for tracking membrane dynamics in live cells²⁰. The results, as depicted in Fig. 2d, e, are consistent with expectations: As the particle diameter decreased, the contrast of iPSF exhibited a discernable reduction, leading to a higher fluctuation in the estimated axial position. The standard deviation of localization fluctuation reached 2.7 nm for 40 nm nanoparticles, compared with 1.6 nm for 200 nm nanoparticles (Fig. 2d).

In addition to localizing static nanoparticles to test the axial localization sensitivity, the proposed approach is also applicable for 3D tracking of dynamic nanoparticles. We conducted a diffusion experiment in which gold nanoparticles were allowed to move freely in water. The total recording duration was 1 s with 4800 frames at a frame rate of 4.8 kHz. For axial localization, the nanoparticle displacement estimated by the analytical

fitting method is shown in Fig. 3a. Template matching based on LSE was also applied as a benchmark. The average localization deviation between the proposed method and template matching using LSE was 1.4 nm (Fig. 3a, inset), which is close to the noise level of localizing the same type of nanoparticles when they were static (Fig. 2b). Figure 3b provides an example of the experimental iPSF and the fitting result.

In order to facilitate 3D trajectory tracking, we also applied RVT to convert the iPSF patterns into single bright spots²⁷. Subsequently, the x-y positions of the converted bright spots were determined by *trackpy*^{28,32}. The estimated 3D trajectory is plotted in Fig. 3c. The proposed analytical model took 36.2 s to track the movement of a single nanoparticle over 4800 frames (53×53 pixels), while the template-matching methods took around 2 h, which demonstrates the high efficiency of the proposed method.

High-speed iSCAT imaging of nanoparticle displacement accurately revealed thermal energy deposition

To assess the accuracy and reliability of the proposed model, we conducted a thermal energy deposition experiment. PDMS, a silicone elastomer widely used in various scientific applications³³, was selected as the material for this experiment due to its well-characterized thermal and mechanical properties. Staining PDMS with red dye allows it to absorb blue light and generate heat, resulting in thermal expansion³⁴. The thermal expansion can be estimated with high accuracy using finite element modeling, given the deposited light energy and the sample geometry³⁵. To experimentally measure the thermal deformation during the photothermal effect and the subsequent recovery due to heat dissipation, nanoparticles were immobilized on the PDMS surface. Their movements were recorded using high-speed iSCAT imaging and processed using the analytical fitting method. The detailed design of the PDMS structure and the experimental parameters are elaborated in *Methods* and Supplementary Methods, Section VI.

To better observe the thermal expansion and recovery, we applied a blue laser with an illumination intensity of 0.23 W/cm^2 and pulse duration of 100 ms. The total recording time was 1500 ms with 15,000 frames at a frame rate of 10 kHz. The processing time for this large number of frames was capped at 45 s for a single nanoparticle, underscoring the efficiency of the proposed tracking method.

The laser source was aligned to achieve a uniform heating within the FOV of iSCAT, theoretically ensuring identical PDMS deformation in the FOV. We heated the PDMS substrate from the top, while its bottom surface embedded with nanoparticles faced down towards the microscope objective. We applied glucose solution that matched the refractive index of PDMS in between the PDMS and the glass coverslip at the bottom to avoid unwanted back reflection in iSCAT. To remove the remaining background unevenness

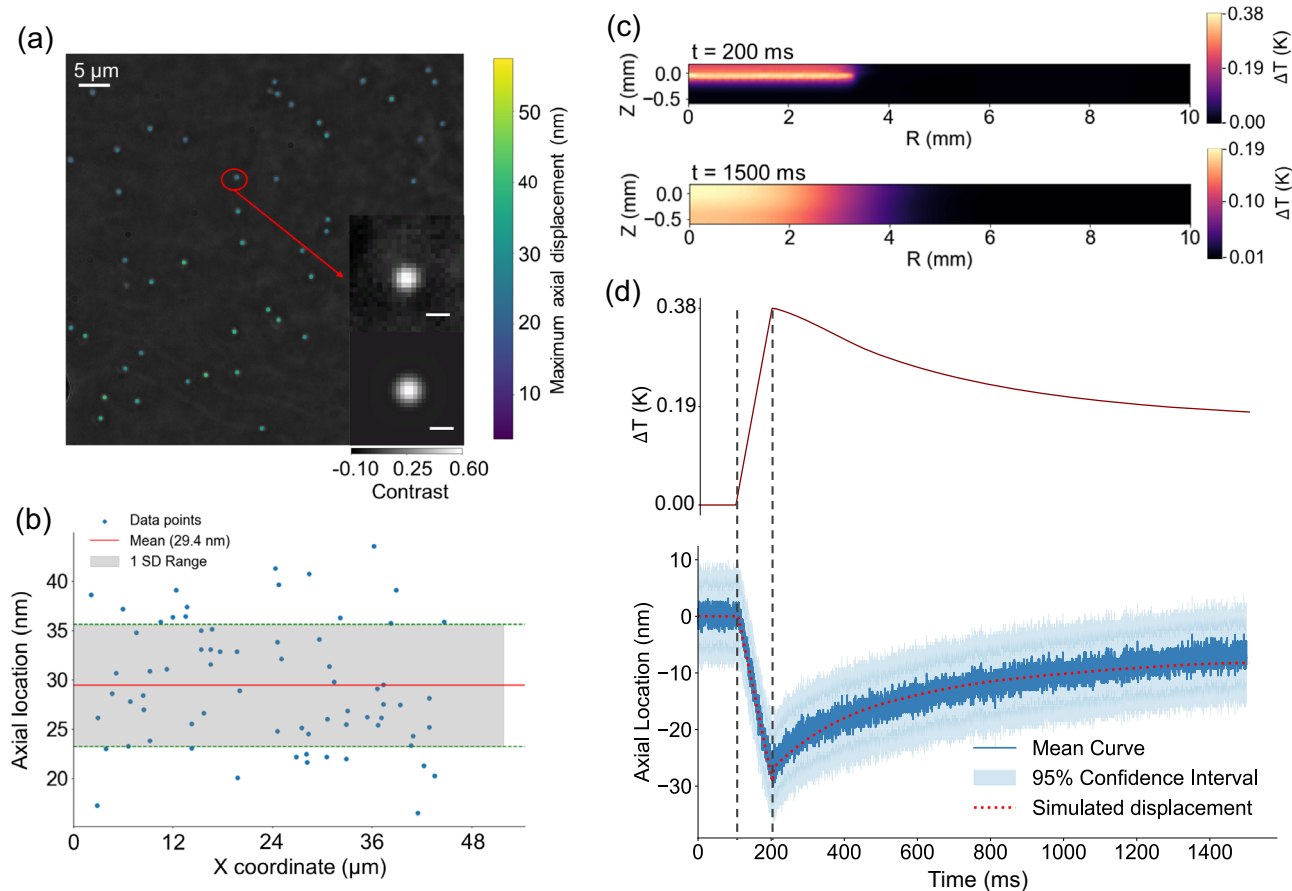


Fig. 4 | The results of the thermal expansion experiment. **a** The estimated maximum displacement of multiple nanoparticles in a wide field and an example of the experimental iPSF (upper) and its corresponding fitting result (lower). Scale bar: 1.5 μm . **b** The scatter plot of the nanoparticles' maximum displacements in (a), where the x-axis represents the x-coordinate of the nanoparticles. The mean value of the maximum displacements is 29.4 nm. **c** The temperature distributions when the laser

pulse ended at $t = 200$ ms (upper) and when the recording ended at $t = 1500$ ms (lower) simulated by finite element modeling. **d** The temperature variation at the center point on the top PDMS surface during the heating and recovery process (upper) and the averaged axial displacement of the nanoparticles (lower). The simulated bottom PDMS surface displacement is shown as the dashed red curve. The heating started at $t = 100$ ms and ended at $t = 200$ ms.

in the iSCAT image, a high-pass Gaussian spatial filter was applied to remove the low spatial frequency components that corresponded to the background unevenness.

Figure 4a illustrates a spatially filtered iSCAT image of multiple nanoparticles within a $48 \mu\text{m} \times 48 \mu\text{m}$ FOV, where the color represents the maximum displacement after heating the sample. In the inset, an example of a target iPSF and its corresponding fitting result is provided. Furthermore, the scatter plot in Fig. 4b validates the consistency of the displacement measurements observed in Fig. 4a. Statistical analysis revealed that the mean maximum displacement of all nanoparticles was 29.4 nm, with a standard deviation of 6.2 nm.

The initial 100 ms of the recording remained unheated for reference, while the heating process started at $t = 100$ ms and ended at $t = 200$ ms. Figure 4c illustrates the simulated heat distribution in the sample at two critical moments: the moment when the heating pulse ended and the moment when the recording concluded. Figure 4d presents the 1D temperature variation at the center point on the top surface of PDMS, along with the average displacement curve of all detected nanoparticles. The simulation results show that the temperature reached its peak immediately upon the termination of the heating pulse, followed by a gradual decrease as heat dissipated over time. Additionally, the displacement curve estimated by the simulation is provided for comparison, demonstrating strong agreement between experimental observations and simulation results. Furthermore, the linearity of the estimated displacement observed during the heating process demonstrates the feasibility and reliability of the proposed method. These results revealed that when a pulsed laser heated the PDMS surface,

rapid thermal expansion occurred due to intense and sudden local heating. As the heat dissipation in the lateral dimension was much slower, the nanoparticle displacement exhibited an almost linear relationship with the energy deposited. Such a linear relationship was proposed as interferometric calorimetry by Goetz et al. using quantitative phase imaging and optical coherence tomography³⁵. Once the laser pulse ceased, the thermal expansion began to recover. The low thermal conductivity of PDMS caused heat dissipation to occur at a relatively slow rate^{33,36,37}, leading to a nonlinear and gradual recovery process.

Discussion

This article presents an analytical fitting approach for efficient axial localization of nano-objects in wide-field iSCAT. The proposed method, derived from the Richards-Wolf integral, considers a linear phase shift and a quadratic amplitude change with respect to the nano-object's axial position. Compared with conventional approaches, the proposed method significantly outperformed in terms of speed (60- to 200-fold increase). It also exhibited superior sensitivity in low SNR conditions (<10 dB) compared to template matching using cross-correlation. We demonstrated the sensitivity, dynamic range, and accuracy of the proposed method through simulations and experiments. Intriguingly, the LSE-based methods, including the proposed analytical fitting method, can achieve higher sensitivity than the conventional template matching based on cross-correlation (Figs. 2 and S3).

To implement the methods discussed in this study, a valid diffraction model is critical. In the far-field limit, the scattered field from a point source is often approximated using the Rayleigh model^{38,39}. However, the Rayleigh

approximation neglects the detailed optical properties of the sample, such as the refractive index difference between the medium and the coverslip, which are particularly relevant in microscopy. To ensure accurate modeling of the scattering electric field captured by the detector, this study employed the Richards-Wolf integral, a robust vectorial diffraction model^{6,8,11,13,14,38}. Unlike the Rayleigh model, which assumes a uniform medium and scalar wave propagation, the Richards-Wolf integral rigorously incorporates the effects of refractive index changes and multiple reflections and refractions at interfaces. Our analytical fitting approach was derived from the Richards-Wolf model but requires no complicated computations or iterations. Meanwhile, it also allows for the incorporation of optical aberrations in its modified zero-order Bessel function $J'(r)$ and extrapolation to an arbitrary analytic model of multiple overlapping iPSFs with their centers determined by the RVT method, making it promising for high-throughput 3D tracking of nano-objects in future studies.

Methods

Wide-field iSCAT microscopy

A wide-field iSCAT was constructed for all experiments. The light source was a supercontinuum laser (SuperK FIANIUM FIU-6 OCT, NKT Photonics, A/S, Birkerød, Denmark) with a spectrum truncated between 820 nm and 840 nm using a band pass filter (FBH830-10, Thorlabs Inc.). The beam was guided to the back focal plane of the objective lens through two pairs of afocal telescopes and the polarizing beamsplitter (CCM1-PBS252/M, Thorlabs Inc.). To enhancing the detection sensitivity of the system to scattered signals and effectively mitigating unwanted background, a quarter wave plate (AQWP10M-580, Thorlabs Inc.) was installed between the objective and the PBS, working in tandem to refine the polarization state. In the detection path, the collected light was directed to the camera (Phantom VEO1310, Ametek, USA) through an imaging lens (ACT508-1000-A, Thorlabs Inc.). For all experiments, a 20× oil immersion objective (CFI Plan Fluor 20XC MI, Nikon Instruments Inc., NA = 0.75) was employed. The refractive index of the immersion oil (n = 1.51) matched that of the coverslip, which effectively eliminated reflection from the bottom surface and ensured a clear background.

Bayesian estimation of the fixed parameters

Our 3D localization process relies on knowing critical experimental parameters, such as system defocus, nanoparticle size, refractive indices, and NA, to generate an analytical iPSF model, and the Bayesian estimation method was employed at the beginning to obtain the system defocus z_f and the nanoparticle size R for the analytical model. According to Bayes' theorem, prior distributions were assumed for each parameter: normal distributions for the system defocus z_f and particle size R , and a gamma distribution for the noise parameter⁷, which can be mathematically expressed as:

$$\begin{aligned} R &\sim \text{Normal}(\mu_R, \sigma_R), \\ z_f &\sim \text{Normal}(\mu_{z_f}, \sigma_{z_f}), \\ \sigma_{\text{noise}} &\sim \text{Gamma}(\mu_{\sigma_{\text{noise}}}, \sigma_{\sigma_{\text{noise}}}). \end{aligned} \quad (7)$$

For parameter inference, we employed Hamiltonian Monte Carlo (HMC) sampling as implemented in *PyMC*¹⁰. The sampling process involved gradient computation, optimization via automatic differentiation, and posterior sampling for each parameter to obtain its estimated value. During Bayesian estimation, the proposed analytical model was utilized to generate the predictive intensity and define the likelihood function. Subsequently, we performed 10,000 MCMC samples to obtain the posterior distribution and computed the mean estimate for parameter inference. For instance, the optimal estimated result of z_f is:

$$\hat{z}_f = E[z_f] = \frac{1}{N} \sum_{i=1}^N z_f^{(i)}, \quad (8)$$

where N is the number of samples ($N = 10,000$ in the study), and i is the iteration index.

Axial localization of nanoparticles by analytical fitting

For axial localization, the analytical model was fitted to the experimental iPSF pattern by accounting for the linear phase shift and quadratic amplitude shift. The corresponding axial displacement was then determined by minimizing the loss function in Eq. (6). Prior to the fitting process, essential pre-processing steps were performed to enhance the accuracy of the model fitting. In the proposed model, the computed intensity values have physical significance and are expressed in the unit of irradiance, whereas the light intensity recorded by the camera is in digital units. If the camera's gain, quantum efficiency, and the imaging system's total transmittance are well calibrated, such a digital unit can be converted to a physical unit, which allows the model to leverage the additional information in the absolute light intensity. To streamline the process and enhance the adaptability of our method, we opted to forgo this calibration but to normalize the modeled iPSF to the experimental iPSF. Specifically, we linearly rescaled the simulated iPSFs to the experimental ones by their intensity ratio at the center point following the equation,

$$\hat{I}(r, z_p) = \hat{I}_0(r, z_p) * \frac{I(0)}{\hat{I}_0(0, z_p)}, \quad (9)$$

where $\hat{I}_0(r, z_p)$ denotes the modeled iPSF pattern without normalization, $I(r)$ is the experimental iPSF pattern, and $\hat{I}(r, z_p)$ is the modeled iPSF pattern after normalization.

During the fitting process, LSE was employed as the loss function to minimize the sum of squared differences between the normalized intensities of corresponding pixels in the target and modeled images¹¹.

Lateral localization of nanoparticles using RVT and Trackpy

For lateral localization, the interference rings in the iPSF were transformed into a bright spot using RVT²⁷. This approach quantified shape characteristics by calculating the variance of pixel intensities along radial lines emanating from a center point, effectively capturing both local and global ring patterns²⁷. The calculated variance highlighted symmetric patterns by measuring the radial intensity changes. Once the transformation was complete, the resulting bright spot was localized using the *trackpy*²⁸ algorithm as the particles exhibited lateral dynamics. *Trackpy* identified particles by locating local intensity maxima, typically employing band-pass filtering and thresholding to reduce noise and enhance feature visibility. After particle locations were identified, the algorithm linked particles across successive frames by minimizing the total displacement between them, employing methods such as the Crocker-Grier method³² or cost-minimization techniques^{42,43}. This robust algorithm effectively handled noise, accommodated varying particle densities, and supported advanced features such as subpixel localization and trajectory refinement, making it highly suitable for analyzing dynamic systems^{28,32}. For nanoparticles fixed in the lateral direction, a simplified approach could be adopted. Following the RVT, a global threshold was applied to select bright spots, and the center of each spot was determined for all frames using the weighted centroid method⁴⁴ at the subpixel level. The coordinate of the center (x_c, y_c) can be calculated as:

$$x_c = \frac{\sum_{i=1}^N \omega_i \cdot x_i}{\sum_{i=1}^N \omega_i}, y_c = \frac{\sum_{i=1}^N \omega_i \cdot y_i}{\sum_{i=1}^N \omega_i} \quad (10)$$

where (x_i, y_i) is the coordinate of the current pixels within the bright spot, ω_i is the corresponding weight. The intensity of each pixel is applied to compute the weight in this paper.

Imaging static and free-floating nanoparticles in wide-field iSCAT

Nanoparticles with a diameter of 200 nm were immobilized on the coverslip to prevent undesired motion. For analysis, an individual nanoparticle was

manually cropped within a defined ROI measuring 27×27 pixels. The center of the iPSF pattern was aligned with the center of the ROI. The size of each pixel on the sample plane was $0.18 \mu\text{m}$.

For the dynamic tracking of individual nanoparticles in water, large gold nanoparticles with a diameter of 200 nm were utilized to minimize the effects of Brownian motion during particle movement in the solution. This configuration facilitated the deposition of nanoparticles onto the coverslip surface, ultimately resulting in their stationary state. A larger ROI of 53×53 pixels was selected to capture additional interferometric rings caused by the greater axial displacements, thereby enhancing the accuracy of the analytical model fitting.

PDMS sample preparation and thermal expansion experiment

For the thermal experiment, a blue laser diode (PD-01236, Lasertack GmbH, Germany) with 445 nm working wavelength was applied as the heating beam. Our sample was designed so that the iSCAT imaging beam would not pass through the heated region in the PDMS to avoid thermal lensing effect²². In this case, we introduced the heating beam from the top surface of the PDMS while the iSCAT imaging beam came from the bottom. Additionally, the PDMS layer was designed to be sufficiently thick to ensure complete absorption of the heating beam.

For energy deposition through photothermal effect, the main PDMS layer was dyed using a saturated solution of hexane and Oil Red O dye (Cat No. A12989.22, Thermofisher, USA) in a 1:1 weight ratio. Gold nanoparticles with a diameter of 200 nm were attached to the bottom surface of PDMS using a Poly-D-Lysine solution (Cat No. A3890401, Thermofisher, USA). A coverslip placed on the top surface of PDMS constrained its upward expansion. We used two ultrathin tapes to attach the PDMS to another coverslip substrate to create a chamber that allowed PDMS to freely expand downwards. We injected glucose solution into the gap between the PDMS and the substrate to avoid unwanted backreflection in iSCAT imaging. The concentration of the glucose solution was designed to match the refractive index of the PDMS⁴⁵. The detailed experimental parameters are listed in Supplementary Methods, Section VI.

To identify multiple nanoparticles in a wide FOV, the RVT was first applied to convert all iPSF patterns into bright spots. A threshold was then selected to distinguish the bright spots from the dark background, and the lateral positions were determined using the weighted centroid method⁴⁴. After obtaining the centroid position, individual iPSFs were cropped in small ROIs (27×27 pixels) to estimate the axial displacement using the proposed analytical fitting approach.

Data availability

All data needed to evaluate the conclusions in the paper are present in the paper and the Supplementary Information. Three example datasets, corresponding to the static nanoparticle experiment, thermal expansion experiment, and particle diffusion experiment, can be downloaded from <https://github.com/NTU-Ling-lab/fast-iscat>. Additional data pertaining to this paper may be requested from the authors.

Code availability

The algorithm demo for our fast axial localization method can be found at <https://github.com/NTU-Ling-lab/fast-iscat>.

Received: 5 February 2025; Accepted: 30 April 2025;

Published online: 27 May 2025

References

- Hsieh, C.-L., Spindler, S., Ehrig, J. & Sandoghdar, V. Tracking single particles on supported lipid membranes: multimobility diffusion and nanoscopic confinement. *J. Phys. Chem. B* **118**, 1545–1554 (2014).
- Dastjerdi, H. M. et al. Optimized analysis for sensitive detection and analysis of single proteins via interferometric scattering microscopy. *J. Phys. D: Appl. Phys.* **55**, 054002 (2021).
- Dahmardeh, M., Mirzaalian Dastjerdi, H., Mazal, H., Köstler, H. & Sandoghdar, V. Self-supervised machine learning pushes the sensitivity limit in label-free detection of single proteins below 10 kDa. *Nat. Methods* **20**, 442–447, <https://doi.org/10.1038/s41592-023-01778-2> (2023).
- Taylor, R. W. & Sandoghdar, V. Interferometric Scattering (iSCAT) Microscopy and Related Techniques. In *Label-Free Super-Resolution Microscopy* (ed. Astratov, V.) 25–65 (Springer, Cham, 2019).
- Jacobsen, V., Stoller, P., Brunner, C., Vogel, V. & Sandoghdar, V. Interferometric optical detection and tracking of very small gold nanoparticles at a water-glass interface. *Opt. Express* **14**, 405–414 (2006).
- Mahmoodabadi, R. G. et al. Point spread function in interferometric scattering microscopy (iSCAT). Part I: aberrations in defocusing and axial localization. *Opt. Express* **28**, 25969–25988 (2020).
- de Wit, X. M. et al. Precise characterization of nanometer-scale systems using interferometric scattering microscopy and Bayesian analysis. *Appl. Opt.* **62**, 7205–7215 (2023).
- Dong, J., Maestre, D., Conrad-Billroth, C. & Juffmann, T. Fundamental bounds on the precision of iSCAT, COBRI and dark-field microscopy for 3D localization and mass photometry. *J. Phys. D: Appl. Phys.* **54**, 394002 (2021).
- Brooks, N. J., Liu, C.-C. & Hsieh, C.-L. *Spiral phase interferometric scattering microscopy for enhanced 3D particle localization and tracking*.
- Mirzaalian Dastjerdi, H., Gholami Mahmoodabadi, R., Bär, M., Sandoghdar, V. & Köstler, H. PiSCAT: a Python package for interferometric scattering microscopy. *J. Open Source Softw.* **7**, 4024 (2022).
- Richards, B. & Wolf, E. Electromagnetic diffraction in optical systems, II. Structure of the image field in an aplanatic system. *Proc. R. Soc. Lond. Ser. A. Math. Phys. Sci.* **253**, 358–379 (1959).
- Wolf, E. Electromagnetic diffraction in optical systems—I. An integral representation of the image field. *Proc. R. Soc. Lond. Ser. A. Math. Phys. Sci.* **253**, 349–357 (1959).
- Born, M. & Wolf, E. *Principles of optics: electromagnetic theory of propagation, interference and diffraction of light*. (Elsevier, 2013).
- Foreman, M. R. & Török, P. Computational methods in vectorial imaging. *J. Mod. Opt.* **58**, 339–364 (2011).
- Török, P. & Varga, P. Electromagnetic diffraction of light focused through a stratified medium. *Appl. Opt.* **36**, 2305–2312 (1997).
- Haeberlé, O. Focusing of light through a stratified medium: a practical approach for computing microscope point spread functions. Part I: Conventional microscopy. *Opt. Commun.* **216**, 55–63 (2003).
- Phillips, A. C. & Davis, L. E. in *Astronomical Data Analysis Software and Systems IV*. 297.
- Shi, Y., Liu, Y., Sheng, W. & Zhu, D. Imaging through motional scattering layers via PSF reshaping and deconvolution. *Opt. Commun.* **461**, 125295 (2020).
- Aygun, U., Urey, H. & Yalcin Ozkumur, A. Label-free detection of nanoparticles using depth scanning correlation interferometric microscopy. *Sci. Rep.* **9**, 9012 (2019).
- Taylor, R. W. et al. Interferometric scattering microscopy reveals microsecond nanoscopic protein motion on a live cell membrane. *Nat. Photonics* **13**, 480–487 (2019).
- Briechele, K. & Hanebeck, U. D. Template matching using fast normalized cross correlation. In *Optical Pattern Recognition XII* 95–102 (SPIE, 2001). <https://doi.org/10.1117/12.421129>.
- Ober, R. J., Ram, S. & Ward, E. S. Localization accuracy in single-molecule microscopy. *Biophys. J.* **86**, 1185–1200 (2004).
- Preza, C. & Conchello, J.-A. Depth-variant maximum-likelihood restoration for three-dimensional fluorescence microscopy. *JOSA A* **21**, 1593–1601 (2004).
- Aguet, F., Van De Ville, D. & Unser, M. A maximum-likelihood formalism for sub-resolution axial localization of fluorescent nanoparticles. *Opt. Express* **13**, 10503–10522 (2005).

25. Carlin, B. P. & Chib, S. Bayesian model choice via Markov chain Monte Carlo methods. *J. R. Stat. Soc. Ser. B: Stat. Methodol.* **57**, 473–484 (1995).
26. Dimiduk, T. G. & Manoharan, V. N. Bayesian approach to analyzing holograms of colloidal particles. *Opt. Express* **24**, 24045–24060 (2016).
27. Kashkanova, A. D. et al. Precision single-particle localization using radial variance transform. *Opt. Express* **29**, 11070–11083 (2021).
28. Allan Daniel, B. et al. *soft-matter/trackpy: Trackpy v0.5.0*, (2021).
29. Abdul-Rahman, H., Gdeisat, M., Burton, D. & Lalor, M. in *Optical measurement systems for industrial inspection IV*. 32–40 (SPIE).
30. Aldrich, J. Doing least squares: perspectives from Gauss and Yule. *Int. Stat. Rev.* **66**, 61–81 (1998).
31. Horn, R. A. & Johnson, C. R. *Matrix analysis*. (Cambridge university press, 2012).
32. Crocker, J. C. & Grier, D. G. Methods of digital video microscopy for colloidal studies. *J. Colloid Interface Sci.* **179**, 298–310 (1996).
33. Wolf, M. P., Salieb-Beugelaar, G. B. & Hunziker, P. PDMS with designer functionalities—Properties, modifications strategies, and applications. *Prog. Polym. Sci.* **83**, 97–134 (2018).
34. Veysset, D. et al. Interferometric imaging of thermal expansion for temperature control in retinal laser therapy. *Biomed. Opt. Express* **13**, 728–743 (2022).
35. Goetz, G. et al. Interferometric mapping of material properties using thermal perturbation. *Proc. Natl. Acad. Sci. USA* **115**, E2499–E2508 (2018).
36. Zhang, G., Sun, Y., Qian, B., Gao, H. & Zuo, D. Experimental study on mechanical performance of polydimethylsiloxane (PDMS) at various temperatures. *Polym. Test.* **90**, 106670 (2020).
37. Suo, Z. & Hutchinson, J. W. Interface crack between two elastic layers. *Int. J. Fract.* **43**, 1–18 (1990).
38. Bohren, C. F. & Huffman, D. R. *Absorption and scattering of light by small particles*. (John Wiley & Sons, 2008).
39. Lee, I.-B. et al. Determination of the absolute concentration of Rayleigh particles via scattering microscopy. *bioRxiv*, 2024.2006.2008.598040 (2024).
40. Salvatier, J., Wiecki, T. V. & Fonnesbeck, C. Probabilistic programming in Python using PyMC3. *PeerJ Computer Sci.* **2**, e55 (2016).
41. Miller, S. J. The Method of Least Squares. In *The Probability Lifesaver: All the Tools You Need to Understand Chance*. Ch. 24, 625–635 (Princeton University Press, Princeton, 2017).
42. Agarwal, K., Ram, O., Wang, J., Lu, Y. & Katz, J. Reconstructing velocity and pressure from noisy sparse particle tracks using constrained cost minimization. *Exp. Fluids* **62**, 1–20 (2021).
43. Matov, A., Edvall, M. M., Yang, G. & Danuser, G. Optimal-flow minimum-cost correspondence assignment in particle flow tracking. *Comput. Vis. Image Underst.* **115**, 531–540 (2011).
44. Wang, J., Urriza, P., Han, Y. & Cabric, D. Weighted centroid localization algorithm: theoretical analysis and distributed implementation. *IEEE Trans. Wirel. Commun.* **10**, 3403–3413 (2011).
45. Yunus, W. M. & Rahman, A. B. Refractive index of solutions at high concentrations. *Appl. Optics* **27**, 3341–3343 (1988).

Acknowledgements

We would like to acknowledge Profs. P. Török and C. Sheppard for discussion about the theory of the Richards-Wolf integral. We are also grateful to H. You. and X. Koh. for help with experiments involving iSCAT system calibration and nanoparticle solution preparation. This work was funded by grants from National Research Foundation Singapore (NRF-NRFF14-2022-0005, T.L.), the Startup Grant from Nanyang Technological University (T.L.), the Ministry of Education, Singapore under its AcRF Tier 2 Grant (MOE-T2EP30124-0010, T.L.) and AcRF Tier 1 Grant (RS19/20, T.L.; RG28/21, T.L.).

Author contributions

T.L. and L.W. conceived the idea. C.L.A. built the iSCAT setup. L.W. and H.N. conducted numerical simulations. C.L.A., L.W., and H.L. conducted the experiments. L.W. analyzed the data. L.W. and T.L. drafted the manuscript. L.W., C.L.A., H.L., B.W., and T.L. discussed and revised the manuscript. All work was supervised by T.L.

Competing interests

The authors declare no competing interests.

Additional information

Supplementary information The online version contains supplementary material available at <https://doi.org/10.1038/s44310-025-00068-3>.

Correspondence and requests for materials should be addressed to Tong Ling.

Reprints and permissions information is available at <http://www.nature.com/reprints>

Publisher's note Springer Nature remains neutral with regard to jurisdictional claims in published maps and institutional affiliations.

Open Access This article is licensed under a Creative Commons Attribution 4.0 International License, which permits use, sharing, adaptation, distribution and reproduction in any medium or format, as long as you give appropriate credit to the original author(s) and the source, provide a link to the Creative Commons licence, and indicate if changes were made. The images or other third party material in this article are included in the article's Creative Commons licence, unless indicated otherwise in a credit line to the material. If material is not included in the article's Creative Commons licence and your intended use is not permitted by statutory regulation or exceeds the permitted use, you will need to obtain permission directly from the copyright holder. To view a copy of this licence, visit <http://creativecommons.org/licenses/by/4.0/>.

© The Author(s) 2025